Chemical Engineering Journal 423 (2021) 130195

Contents lists available at ScienceDirect

Chemical Engineering Journal

journal homepage: www.elsevier.com/locate/cej

# Silk fibroin-$Ti_3C_2T_X$ hybrid nanofiller enhance corrosion protection for waterborne epoxy coatings under deep sea environment

Junfeng Chen [a,b], Wenjie Zhao [a,*]

[a] Key Laboratory of Marine Materials and Related Technologies, Zhejiang Key Laboratory of Marine Materials and Protective Technologies, Ningbo Institute of Materials Technology and Engineering, Chinese Academy of Sciences, Ningbo 315201, China
[b] University of Chinese Academy of Sciences 19 A Yuquan Rd, Shijingshan District, Beijing 100049, China

ARTICLE INFO

*Keywords:*
Deep sea
$Ti_3C_2T_X$
Silk fibroin
Anti-corrosion
High hydrostatic pressure
Adhesion strength

ABSTRACT

The complex and harsh deep sea environment is the main reason for the failure of the protective coating of marine equipment. However, excellent protective coating is the key to prolong the service life of the equipment under deep sea environment. $Ti_3C_2T_X$, with high aspect ratio, abundant surface functional groups and excellent mechanical properties, is the suitable candidate nanofiller for coating reinforcement. Herein, we synthesized a novel silk fibroin-$Ti_3C_2T_X$ (SF-$Ti_3C_2T_X$) hybrid nanofiller as reinforced-additives for improving the anti-corrosion ability of waterborne epoxy coating. Due to the rough surface of SF-$Ti_3C_2T_X$ nanosheets, they have excellent compatibility with the resin matrix and could fill the inherent defects of the coating. The anticorrosion behaviors of as-prepared composite coatings under both of atmospheric pressure and simulated deep sea environment were investigated in detail. Particularly, the composite coating with 0.5 wt% SF-$Ti_3C_2T_X$ sheets showed outstanding corrosion protection (impedance value remained 1.31 × $10^8$ Ω·$cm^2$, four orders of magnitude higher than pure EP) after 240 h immersion under 20 MPa hydrostatic pressure. In addition, the interface of coating/steel was not damaged and the coating remained the favorable adhesion strength (3.16 MPa, but that of pure EP only 0.88 MPa) even in the harsh high hydrostatic pressure. Based on the experiment data, we discussed and analyzed the failure process of coatings and explained the corrosion protection mechanism of SF-$Ti_3C_2T_X$ hybrid under simulated deep sea environment.

## 1. Introduction

With the exploitation of marine resources, nowadays, the requirements of the engineering equipment in harsh and complex deep sea environment have constantly increased [1]. Compared with ordinary marine environment, the deep-sea environment is specifically characterized with high hydrostatic pressure, dissolved oxygen, water velocity and relatively low temperature, etc. [2]. Among these complex parameters, the hydrostatic pressure greatly affects the corrosion behaviors of metals in deep sea [3]. Therefore, excellent protective materials are critical for the equipment which worked in the deep sea for long-term service. As we known, the organic coating is one of the most effective protection methods for metals in marine environment [4]. Currently, the application of the organic coating in the deep-sea has been widely researched. The research results indicated that high hydrostatic pressure could significantly reduce the protective performance of organic coatings by promoting corrosive medium diffusion in the coating, thus accelerating the damage and failure of the metal substrate [5–7].

Inorganic fillers could improve the physical barrier properties of coating by prolong the diffusion path of electrolyte, for example, glass flake [1], mica [4] and montmorillonite [8]. However, these traditional pigments with low aspect ratio were large additive amount, difficult construction and easy crack, which would avianize the protective effect of the coating. Therefore, it is essential to develop novel nanofillers to endow coating outstanding anticorrosion in deep sea environment [9]. The two-dimensional (2D) materials, with ultra-thin thickness, fascinating water impermeability, superior mechanical properties and high specific surface area, were widely used in the field of metal corrosion protection [10–12]. Therefore, 2D materials are promising to achieve high-quality organic coatings applied in deep-sea environment.

Currently, 2D materials such as graphene (G), graphene derivatives, molybdenum disulfide ($MoS_2$), layered double hydroxides (LDHs) and hexagonal boron nitride (h-BN) were used as fillers to mix with organic coatings for enhancing the corrosion resistance of the composite

* Corresponding author.
*E-mail address:* zhaowj@nimte.ac.cn (W. Zhao).

https://doi.org/10.1016/j.cej.2021.130195
Received 20 February 2021; Received in revised form 18 April 2021; Accepted 30 April 2021
Available online 5 May 2021

coatings in NaCl solution under normal pressure via prolonging the diffusion channel length of corrosion species and promoting the compactness of the coatings [13–17]. Meanwhile, to enhance the interface compatibility of 2D materials and resin, researchers often modify the 2D materials via physical or chemical methods. For example, Ramezanzadeh et al. [18] investigated the functionalization of GO via 3-Aminopropyl triethoxysilane (APTES) as a reinforce-filler for improved the corrosion resistance of epoxy coating, and demonstrated that the adhesion force and protection efficiency were evidently enhanced. Cui et al. [19] discussed the anticorrosion mechanism of hexagonal boron nitride (h-BN) nanosheets modified by carboxylated aniline trimer derivatives, and indicated that only 1 wt% h-BN nanosheets added could hinder the diffusion of electrolyte and improve the protective performance of the coating.

As an attractive 2D material, MXene, with abundant surface functional groups, excellent mechanical properties and good workability, has been widely applied in energy storage, water purification, sensor, electromagnetic shielding and catalysis [20–24]. The chemical formula of MXene could be expressed as $M_{n+1}X_nT_X$ (n=1~3), M, X and $T_X$ represent early transition metal elements, carbon or nitrogen elements, and the surface terminations, such as –OH, –O and –F, respectively [25,26]. Presently, over 20 kinds of MXene materials have been reported and the corresponding application have been researched [27]. Among them, $Ti_3C_2T_X$ was the earliest and most widely studied 2D materials [25]. Few-layer $Ti_3C_2T_X$ nanosheets displayed fine flexibility, large specific surface area and excellent mechanical properties, which was often applied to composites for improving properties of matrix [28]. Compared with graphene and graphene derivative, $Ti_3C_2T_X$, with abundant surface terminals, was a promise candidate for application in promoting the anticorrosion performance of organic coatings. According to previous reports, Yan et al. [29] explored the corrosion resistance of the $Ti_3C_2T_X$/epoxy coating, and proved that the corrosion current density of the $Ti_3C_2T_X$/epoxy composite coating decreased by one to two orders of magnitude compared with pure epoxy coating.

Generally, chemical compatibility and dispersion ability of nanosheets with epoxy coating was crucial to improve the protection ability of the composite coating [30]. The active terminals on the surface of $Ti_3C_2T_X$ nanosheets provided the possibility of further functionalization, thereby achieving well compatibility with epoxy matrix. Fan et al. [31] employed 3-aminopropyl triethoxysilane functionalized $Ti_3C_2T_X$ nanosheets via covalent interactions to significantly improve the dispersion of nanosheets in epoxy resin. They stated that the composite coating with 0.5 wt% amino-functionalized $Ti_3C_2T_X$ nanofiller exhibited excellent anticorrosion performance. Besides, Fan's group prepared the wrapping structure of $Ti_3C_2$/G hybrid by the "bridge" effect of polydopamine of functionalization $Ti_3C_2T_X$ [32]. Owning to the synergistic effect of $Ti_3C_2$ and graphene, the composite coating could display the outstanding anticorrosion properties. However, despite these reports, the long term anticorrosion mechanism of $Ti_3C_2T_X$ was not fully revealed. In addition, to the best of our knowledge, the MXene materials haven't been studied in the field of deep-sea protective coatings. Thus, it has great significance to thoroughly explore the corrosion resistance and corresponding mechanism of $Ti_3C_2T_X$ MXene as nanofillers under deep sea environment.

Silk fibroin (SF), a natural macromolecular fibrin produced by Bombyx mori silkworms, exhibits outstanding mechanical properties, good biocompatibility and controllable biodegradability [33,34]. Notably, the amino acid residues on the protein can covalently interact with the functional groups on the surface of $Ti_3C_2T_X$ nanosheets.

Herein, we report the synthesis of silk fibroin-$Ti_3C_2T_X$ hybrid nanosheets (SF-$Ti_3C_2T_X$) and incorporate it into waterborne epoxy matrix for constructing high-performance anticorrosion composite coating applied to deep-sea high hydrostatic pressure for the first time. The anticorrosion behaviors of as-prepared composite coatings were investigated by electrochemical impedance spectroscopy measurements in 3.5 wt% NaCl solution under atmospheric pressure and 20 MPa hydrostatic pressure, respectively. Further, we observe the corrosion products and coating/steel interface to discuss the anticorrosion mechanism. In addition, we measure the tensile strength and adhesion strength to consider mechanical properties of coatings. The anti-corrosion behaviors and mechanism of the composite coating was analyzed and discussed comprehensively. We aimed to fabricate high-performance SF-$Ti_3C_2T_X$/EP coating for achieving effective protection to metal in deep sea environment.

## 2. Materials and method

### 2.1. Materials

$Ti_3C_2T_X$ powder was provided by Nanjing Xianfeng nano materials Co. Ltd. Trimethylphenylammonium hydroxide (PTAH) (8% dissolved in methanol) was provided by Ti xi'ai (Shanghai) Chemical Industry Development Co. Ltd. 4-dimethylaminopyridine (DMAP) and Catalyst 1-(3-(dimethylamino)propyl)-3-ethyl carbimide hydrochloride (EDC) were purchased from Aladdin Regent Co. Ltd. Anhydrous ethanol and acetone was purchased from Sinopharm Chemical Reagent Co. Ltd. Silk fibroin was provided by Chengdu YoungShe Chemical Co. Ltd. Waterborne epoxy resin and curing agent were provided by Shanghai Runtan New Material Technology Co. Ltd. China. The Q235 steel , with the area of 1*1 $cm^2$, were polished by $400^{\#}$, $800^{\#}$, and $1200^{\#}$ sandpapers and ultrasonically cleaned by anhydrous ethanol.

### 2.2. Synthesis of silk fibroin-modified $Ti_3C_2T_X$ (SF-$Ti_3C_2T_X$)

The few-layer $Ti_3C_2T_X$ (f-$Ti_3C_2T_X$) nanosheets were prepared according to the alternating pressure assisted method [35]. Specifically, after multilayer $Ti_3C_2T_X$ was pre-intercalated with PTAH, it was put into the autoclave and the few-layered nanosheets were obtained by using the "press-tear" action of alternating pressure. Furthermore, SF-$Ti_3C_2T_X$ was prepared via esterification reaction between silk fibroin protein and hydroxyl group on $Ti_3C_2T_X$, as shown in Fig. 1a. Briefly, the f-$Ti_3C_2T_X$ and silk fibroin were dispersed in deionized water (weight ratio of 3:1). The catalyst consisting of EDC and DMAP (6 mg, weight ratio of 1:1) was added into the silk fibroin/f-$Ti_3C_2T_X$ suspension to facilitate the reaction. After reacting at 60 °C for 3 h at $N_2$ atmosphere, the SF-$Ti_3C_2T_X$ was obtained. For further use and characterization, the SF-$Ti_3C_2T_X$ suspension was washed with DI water and centrifuged at 10,000 r/min three times. Finally, SF-$Ti_3C_2T_X$ powder was collected by freeze-drying method.

### 2.3. Fabrication of SF-$Ti_3C_2T_X$/EP composite coatings

SF-$Ti_3C_2T_X$/epoxy composite coatings were fabricated as follows: (a) 12 g waterborne epoxy resin was mixed with the SF-$Ti_3C_2T_X$ ethanol dispersion, and then was ultrasonic for 30 min; (b) the mixture was stirred under 1500 r/min for 6 h to form a homogeneous dispersion of SF-$Ti_3C_2T_X$/epoxy; (c) 6 g curing agent was added into the above epoxy solution and stirred 10 min; (d) the mixture was painted on the Q235 electrodes via a wire bar coater (the thickness of the coating was fixed at 40 ± 5 μm); (e) the coated composite coatings were cured at ambient temperature for 48 h. The additive amounts of SF-$Ti_3C_2T_X$ were 0.25 wt %, 0.5 wt% and 0.75 wt%, and the as-prepared samples were denoted as 0.25SF-$Ti_3C_2T_X$/EP, 0.5SF-$Ti_3C_2T_X$/EP, and 0.75SF-$Ti_3C_2T_X$/EP, respectively. By comparison, the pure epoxy coating and 0.5f-$Ti_3C_2T_X$/EP composites coating were prepared through a similar method. The as-prepared coatings were brittlely broken by liquid nitrogen before SEM test to obtain the cross section of the coating.

### 2.4. Characterizations

The structure of the $Ti_3C_2T_X$ nanosheet was performed by X-ray powder diffraction (XRD, D8 ADVANCE, Bruker) with Cu $K_\alpha$ radiation

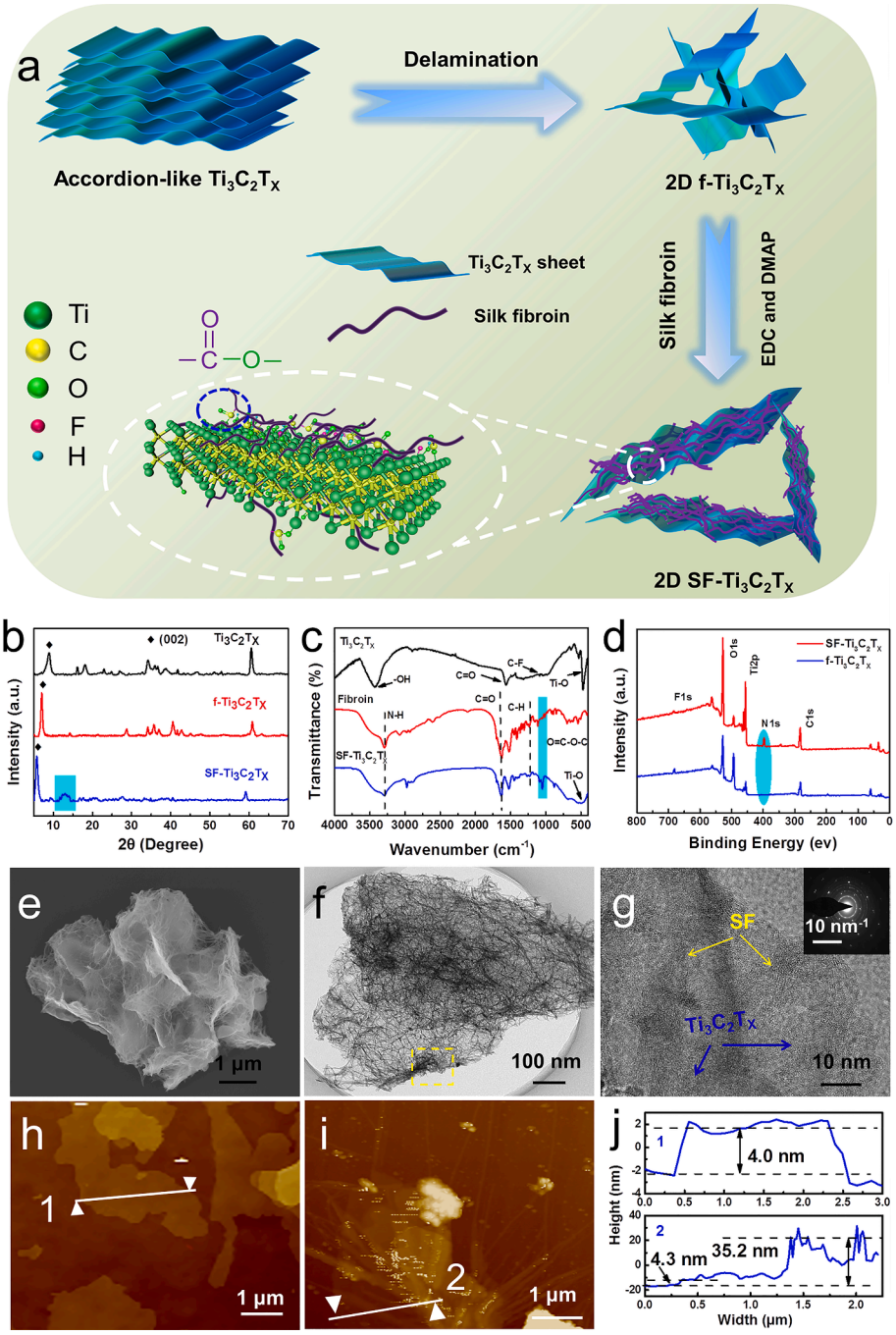


**Fig. 1.** The schematic representation of the SF-$Ti_3C_2T_X$ synthesis procedure (a); (b) XRD pattern; (c) FTIR pattern; (d) XPS pattern; (e) SEM image, (f) TEM image and (g) HRTEM image of SF-$Ti_3C_2T_X$; (h) SPM image of f-$Ti_3C_2T_X$; (i) SPM image of SF-$Ti_3C_2T_X$; (j) height profiles of the cross section of f-$Ti_3C_2T_X$ and SF-$Ti_3C_2T_X$.

from 5° to 80°. The chemical structure of $Ti_3C_2T_X$ nanosheets was recorded by a Fourier transform infrared spectrophotometer (FTIR, Nicolet 6700) with a range of 400–4000 $cm^{-1}$ and an X-ray photoelectron spectroscopy (XPS, Axis Ultra DLD). Thermogravimetric analysis (TG, Diamond TG/DTA, PerkinElmer) was performed in $N_2$ atmosphere with 5 °C min heating rate from 40 °C to 800 °C. The surface morphology and thickness of the $Ti_3C_2T_X$ nanosheet were observed via a field emission scanning electron microscope (FE-SEM, Hitachis-4800), a transmission electron microscope (TEM) system (Talos F200x) and a scanning probe microscope (SPM) system (Dimension 3100). The fracture morphology of coatings was observed by SEM. The corrosion products were observed by SEM (FEG 250). An adhesion tester (PosiTest AT-M Adhesion tester) was employed to estimate adhesion strength of the composite coatings.

### 2.5. Electrochemical measurements

The corrosion resistance of the $Ti_3C_2T_X$/EP coated electrodes was investigated by an electrochemical workstation (Gamry) with traditional three-electrode system (working electrode was painted Q235 electrode, counter electrode was platinum electrode and the saturated calomel electrode (SCE) and solid Ag/AgCl electrode was treated as reference electrode under atmospheric pressure and 20 MPa hydrostatic pressure, respectively). The electrochemical impedance spectroscopy (EIS) was measured in the frequency range of $10^{-2}$-$10^5$ Hz using sinusoidal perturbation with an amplitude of 20 mV. Moreover, the recorded

EIS results were fitted by the ZSimpWin software to obtain detailed corrosion data. To ensure repeatability, at least three parallel samples were prepared and tested for all samples. In addition, to survey the local corrosion of steel substrate beneath the composite coatings, a local electrochemical impedance spectroscopy (LEIS, AMETEK) was applied (coatings with an about 2 mm artificial defect). The local impedance of the samples was detected at a frequency of 1 kHz in the range of 4 × 4 $mm^2$. During the corrosion resistance evaluation, all samples were immersed in the 3.5 wt% NaCl solution.

## 3. Results and discussion

### 3.1. Characterization of SF-$Ti_3C_2T_X$

XRD patterns exhibited the evolution of crystalline structure during the delamination process of $T_3C_2T_X$ and synthesis of SF-$Ti_3C_2T_X$, as shown in the Fig. 1b. After the intercalation and delamination, the characteristic peak (0 0 2) of f-$Ti_3C_2T_X$ moved negatively from 8.95° to 7.06°, indicated that the interlayer spacing of f-$Ti_3C_2T_X$ expanded significantly. The characteristic peak (0 0 2) was shifted to smaller angle (2θ = 5.79°) after modification via SF and a steamed bread peak appeared at around 2θ = 14°. This was attributed to the attachment of SF fibers to the f-$Ti_3C_2T_X$ nanosheets, which led to the structural change. Meanwhile, the FT-IR pattern demonstrated the SF-$Ti_3C_2T_X$ was successfully synthesized. The FT-IR spectra of f-$Ti_3C_2T_X$, SF and SF-$Ti_3C_2T_X$ were shown in Fig. 1c. Obviously, the typical characteristic bands of f-$Ti_3C_2T_X$ could be observed at approximately 3425, 1639 and 535 $cm^{-1}$, which were ascribed to the stretching vibration of –OH, C=O and Ti-O, respectively. After modified by silk fibroin fiber, compared with the f-$Ti_3C_2T_X$, new characteristic absorption bands of SF-$Ti_3C_2T_X$ could be presented at ~ 3300, ~1640 and ~ 1235 $cm^{-1}$, which were associated with N–H, C=O and C-N peak, respectively. These characteristic peaks suggested the existence of the silk fibroin fiber. Significantly, the absorption bands related to the ester bonds appeared at ~ 1089 and ~ 1048 $cm^{-1}$, indicating the successful esterification reaction between silk fibroin fiber and $T_3C_2T_X$ nanosheets [36,37].

The chemical structure of the SF-$Ti_3C_2T_X$ was further explored via the XPS. The full spectra of f-$Ti_3C_2T_X$ and SF-$Ti_3C_2T_X$ were displayed in Fig. 1d, which proved the existence of Ti 2p (455.9 eV), C 1 s (285.0 eV), O 1 s (531.2 eV) and F 1 s (684.6 eV). Especially, the full spectra of SF-$Ti_3C_2T_X$ exhibited a new N 1 s (400.8 eV) peak compared with f-$Ti_3C_2T_X$, ascribed to the N element presenting in SF fibers. Moreover, the fine spectrum of C 1 s of f-$Ti_3C_2T_X$ and SF-$Ti_3C_2T_X$ were shown in Fig. S1b and Fig. S1c. The C 1 s core-level pattern could be curve-fitted with five peak components, including 279.6 eV (C-Ti), 283.4 eV (C=C), 283.6 eV (C–C), 284.3 eV (C-O), 286.2 eV (C-F) [37,38]. After modification by SF, new-emerging peaks approximately appeared at 284.6 eV and 288.1 eV assigning to the C-N bond and the O-C=O peak in C 1s spectra of SF-$Ti_3C_2T_X$, which illustrated the successful esterification reaction between the hydroxyl groups of $Ti_3C_2T_X$ nanosheets and carboxyl groups of SF fibers.

To observe the morphology changes of modified $Ti_3C_2T_X$ intuitively, the $Ti_3C_2T_X$ nanosheets were characterized by SEM. The typical accordion-like structure of $Ti_3C_2T_X$ was demonstrated in Fig. S1d. Evidently, after delamination, the accordion-like structure of $Ti_3C_2T_X$ was transformed into a typical 2D layered structure with larger specific surface area, as shown in Fig. S1e. And the surface of the nanosheet was smooth and angular. Significantly, the surface of the nanosheet was covered by network material after being modified via SF fibers and the surface became rough, as illustrated in Fig. 1e. In addition, rough surface would be beneficial for the adhesion strength between the $Ti_3C_2T_X$ nanosheets and epoxy resin, which could form composite materials with higher compactness and better mechanical properties. Meanwhile, TEM and SPM images could further confirmed morphology and structure features of the SF-$Ti_3C_2T_X$ nanosheet. The f-$Ti_3C_2T_X$ nanosheet was almost transparent and the stacking of the few-layer could be discovered easily, implying a high degree of delamination for thinness, as shown in Fig. S1f. However, a rough and opaque appearance, as well as network material, was manifested for the SF-$Ti_3C_2T_X$ hybrid, which could be attributed to the attachment of SF fibers, as shown in Fig. 1f. Meanwhile, the high resolution transmission electron image (HRTEM) and selected area diffraction pattern (SAED) of SF-$Ti_3C_2T_X$ nanosheet were shown in the Fig. 1g. The HRTEM region of SF and f-$Ti_3C_2T_X$ could be distinguished easily, indicating that SF had attached on $Ti_3C_2T_X$ nanosheets successfully. Moreover, diffraction spots with order arrange in a hexagonal were bright and the polycrystalline diffraction rings were displayed, indicating that the SF-$Ti_3C_2T_X$ maintained the crystal integrity, which meant that the reaction didn't destroy the crystal structure of the $Ti_3C_2T_X$. These features suggested that the SF fibers were successfully combined with $Ti_3C_2T_X$. As a microscopic characterization technique, the SPM was also applied to characterize the morphology and thickness of the lamellar. As shown in Fig. 1h and 1i, f-$Ti_3C_2T_X$ exhibited quintessential flaky structures without the visible aggregation and its surface was smooth. Moreover, the thickness of f-$Ti_3C_2T_X$ was about 4.0 nm according to the corresponding height profiles of the cross section, as shown in Fig. 1j. On the contrary, the SF-$Ti_3C_2T_X$ nanosheet displayed the uneven and rough surface morphology and the thickness was increased to 35.2 nm due to the presence of SF fibers.

### 3.2. Physical properties of the composite coatings

To discuss the dispersion ability and interface compatibility between SF-$Ti_3C_2T_X$ nanosheets and epoxy resin, the cross-sectional morphologies of as-prepared composites coatings were observed. The fracture morphology of pure EP displayed clear pinholes and defects, which were ascribed to the rapid evaporation of solvent during the curing process of the coating [39], as shown in Fig. 2a. In addition, the contact angle of pure coating and composites coatings were measured. A lower contact angle value of 66.9° was exhibited for the pure EP. The introduction of f-$Ti_3C_2T_X$ nanosheets into the EP matrix caused a relatively rough morphology and few holes and showed a higher contact angle (77.9°), as shown in Fig. 2b. Obviously, after incorporating SF-$Ti_3C_2T_X$ hybrid into the EP matrix, the fracture surface was more uniform hardly with defects (Fig. 2c, 2d and 2e), suggesting that the SF-$Ti_3C_2T_X$ hybrid could enhance the compactness and integrity of composite coatings. Particularly, as the addition of SF-$Ti_3C_2T_X$ was 0.5 wt%, the cross sectional morphology was the most uniform without any defects. For the contact angle, higher values were observed (89.4°, 99.8° and 92.7° attributed to the 0.25SF-$Ti_3C_2T_X$/EP, 0.5SF-$Ti_3C_2T_X$/EP and 0.75SF-$Ti_3C_2T_X$/EP, respectively). This may be attributed to the change of surface chemical state caused by the incorporation of SF-$Ti_3C_2T_X$ nanosheets. The coating with larger contact angle could better resist the corrosive medium than those with a lower contact angle. Based on these results, it was confirmed that the SF fibers effectively improved the compatibility between $Ti_3C_2T_X$ and EP matrix.

To further investigate the effect of nanofillers on the property of the $Ti_3C_2T_X$/EP composite coatings, their mechanical behaviors were evaluated. The tensile strength of the composite coating was exhibited in Fig. S2a. Evidently, the addition of $Ti_3C_2T_X$ nanofillers improved the tensile strength of the coating. With the introduction of f-$Ti_3C_2T_X$, the tensile strength of the composite coating was 9.31 MPa (3.7 MPa higher than that of the pure EP), which was attributed to the improved density and integrity of the composite coating to a certain extent. However, f-$Ti_3C_2T_X$ was difficult to improve the mechanical properties of the coating due to the smooth and flat surface of the nanosheet. Remarkably, benefiting from the modification f-$Ti_3C_2T_X$ nanosheet by SF fibers, the as-prepared composite coatings exhibited a dramatically enhanced mechanical performance. Especially, the tensile strength of 0.5SF-$Ti_3C_2T_X$/EP composite coating was 184.5% and 72.1% higher than that of the EP and f-$Ti_3C_2T_X$/EP, respectively. This was ascribed to the favorable interface compatibility between SF-$Ti_3C_2T_X$ nanosheets and EP matrix.

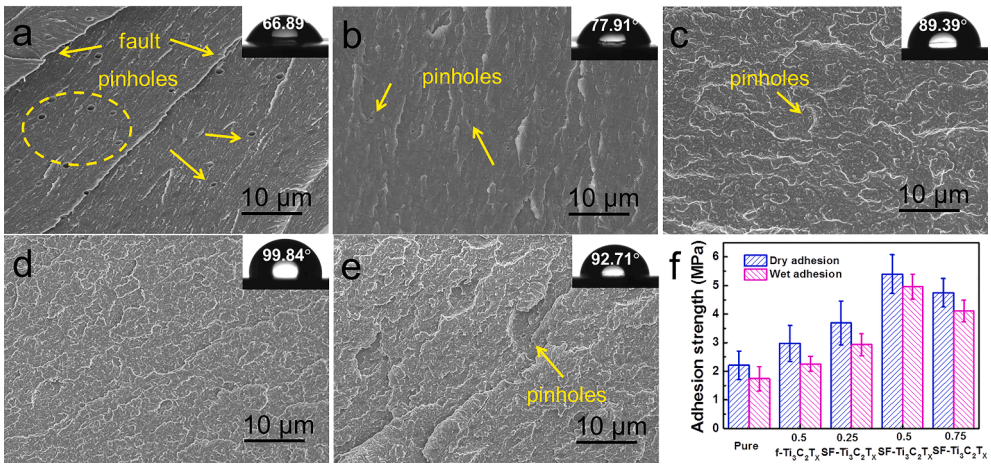


**Fig. 2.** The cross-sectional morphologies of (a) pure EP, (b) 0.5f-$Ti_3C_2T_X$/EP, (c) 0.25SF-$Ti_3C_2T_X$/EP, (d) 0.5SF-$Ti_3C_2T_X$/EP and (e) 0.75SF-$Ti_3C_2T_X$/EP; (f) the adhesion strength of composite coatings.

In addition, the adhesion strength of the coating with the substrate was one of the key indicators to estimate the anti-corrosion ability of the coating [40]. Therefore, pull-off test was employed to evaluate the adhesion strength of the as-prepared SF-$Ti_3C_2T_X$ composite coating, as illustrated in Fig. 2f. Obviously, $Ti_3C_2T_X$ nanosheets could improve the adhesion strength of a coating on the Q235 steel whether under atmospheric conditions or under wet conditions (immersion in the 3.5 wt% NaCl solution for 48 h). The adhesion strength of pure EP was 2.21 MPa and 1.74 MPa under dry and wet condition, respectively. For the f-$Ti_3C_2T_X$/EP, the adhesion strength was 2.94 MPa (dry) and 2.25 MPa (wet), respectively. Although the adhesion strength could be improved to some extent, the poor dispersion limited the enhancement effect. Compared with f-$Ti_3C_2T_X$/EP, the adhesion strength of 0.5SF-$Ti_3C_2T_X$/EP was increased by 85.3% (dry) and 120.8% (wet), respectively, which meant that SF-$Ti_3C_2T_X$ could effectively optimize the integrity of the coating and facilitated the adhesion. The introduction of strong adhesion force prevented the coating exfoliation from the substrate, which granted the composite coating with favorable protection performance under deep-sea hydrostatic pressure.

### 3.3. *Anti-corrosion performances of the $Ti_3C_2T_X$/EP composite coatings*

The corrosion resistance of the $Ti_3C_2T_X$/EP composite coating with different immersion periods was evaluated via EIS measurement. As shown in Fig. 3, the Nyquist and Bode plots of the Q235 steel coated with the composite coatings under atmospheric pressure in 3.5 wt% NaCl solution were presented. In the Nyquist plot (Fig. 3a-3e), a large diameter of capacitive impedance arc represents an excellent anticorrosion performance [41]. Obviously, the diameter of capacitive impedance arc of all coatings displayed the shrunken trend during 60 days of immersion, explaining that the protection ability of coatings had been declined. In the case of pure EP, the phenomenon of diffusion emerged after the 20 days of immersion, indicating that the corrosive medium (such as $H_2O$, $Cl^-$ and $O_2$) diffused to the interface of the coating and the metal substrate through the defects in the coating. However, for the 0.5f-$Ti_3C_2T_X$/EP, Nyquist data displayed two capacitive arcs after the 60 days of immersion, suggesting that the corrosion channel did not fully opened and the coating had certain protective effects. Notably, SF-$Ti_3C_2T_X$/EP still exhibited the large capacitive impedance arc diameter and without diffusion phenomenon. The capacitive arc diameter of 0.25SF-$Ti_3C_2T_X$/EP and 0.75SF-$Ti_3C_2T_X$/EP were less than 0.5SF-$Ti_3C_2T_X$/EP. This meant that SF-$Ti_3C_2T_X$ hybrid could enhance the compactness of resin matrix and provide the excellent physical shielding effect, which made the coating maintain the excellent protective performance after the long-time immersion.

In general, low frequency impedance modulus ($|Z|_{0.01\ Hz}$ Fig. 3f-3j) was as a half quantitative index to evaluate the anticorrosion properties of the coating [42]. At the initial immersion stage, pure EP and 0.5f-$Ti_3C_2T_X$/EP showed the lower impedance ($6.65 \times 10^8\ \Omega{\cdot}cm^2$ and $8.26 \times 10^8\ \Omega{\cdot}cm^2$, respectively). With the extension of immersion time, the $|Z|_{0.01\ Hz}$ value of pure EP and 0.5f-$Ti_3C_2T_X$/EP fell sharply, showing that the poor barrier ability and protection performance of the coating. However, the $|Z|_{0.01\ Hz}$ of (0.25, 0.5, 0.75)SF-$Ti_3C_2T_X$/EP kept at a high level during the whole immersion time, indicating that the SF-$Ti_3C_2T_X$ hybrid nanofillers could full play to the "maze effect" and prolong the diffusion channel of corrosive ions. In addition, the $|Z|_{0.01\ Hz}$ of 0.5SF-$Ti_3C_2T_X$/EP was the highest one (from $2.31 \times 10^9\ \Omega{\cdot}cm^2$ to $7.8 \times 10^8\ \Omega{\cdot}cm^2$), suggesting the strongest protection capability for steel substrate.

The high hydrostatic pressure could accelerate the deterioration process of the organic coating [7]. The anti-corrosion effectiveness of SF-$Ti_3C_2T_X$/EP in the high hydrostatic pressure environment was analyzed via EIS measurement. The OCP of the samples under 20 MPa hydrostatic pressure was measured as a function of immersion time and the results were shown in Fig. 4. Notably, the OCP of all the samples significantly showed a decrease in about 0–48 h. Especially, the descend range of OCP of pure EP was the largest (from −113.4 mV (vs. Ag/AgCl) to −432 mV (vs. Ag/AgCl)). This phenomenon could be explained that serious invasion of the coating occurred by corrosive ions during this period under hydrostatic pressure. Moreover, the significant decrease of OCP of pure EP was appeared again from 96 h, suggesting that the corrosion channel was open and the coating failure was accelerated. The 0.5f-$Ti_3C_2T_X$/EP exhibited a similar downward trend, but the second decline was delayed, indicating that f-$Ti_3C_2T_X$ nanofillers could defer the invasion of corrosive medium to a certain extent. However, the variation of 0.5SF-$Ti_3C_2T_X$/EP's OCP was the slightest during the whole immersion time (from −93.2 mV (vs. Ag/AgCl) to −289 mV (vs. Ag/AgCl)), illustrating that the SF-$Ti_3C_2T_X$ could endow the coating displayed a slower failure process and a greater protective performance in deep sea environment.

According to the impedance plots, the failure process and anti-corrosion effectiveness of the coating was studied, as shown in the Fig. 5. Evidently, the capacitive arcs of all the coatings appeared a shrunken trend in the 240 h immersion time, demonstrating that high hydrostatic pressure could accelerate the failure of coatings. For the pure EP, there was a diffusion arc at the low frequency region after 48 h immersion, as shown in Fig. 5a. This phenomenon could be considered that corrosive medium (such as $H_2O$, $Cl^-$ and $O_2$) through the coating to the coating/metal interface via high hydrostatic pressure. With the time prolongation, electrochemical reaction sustainably occurred and resulted in the accumulation of corrosion products at the coating/metal

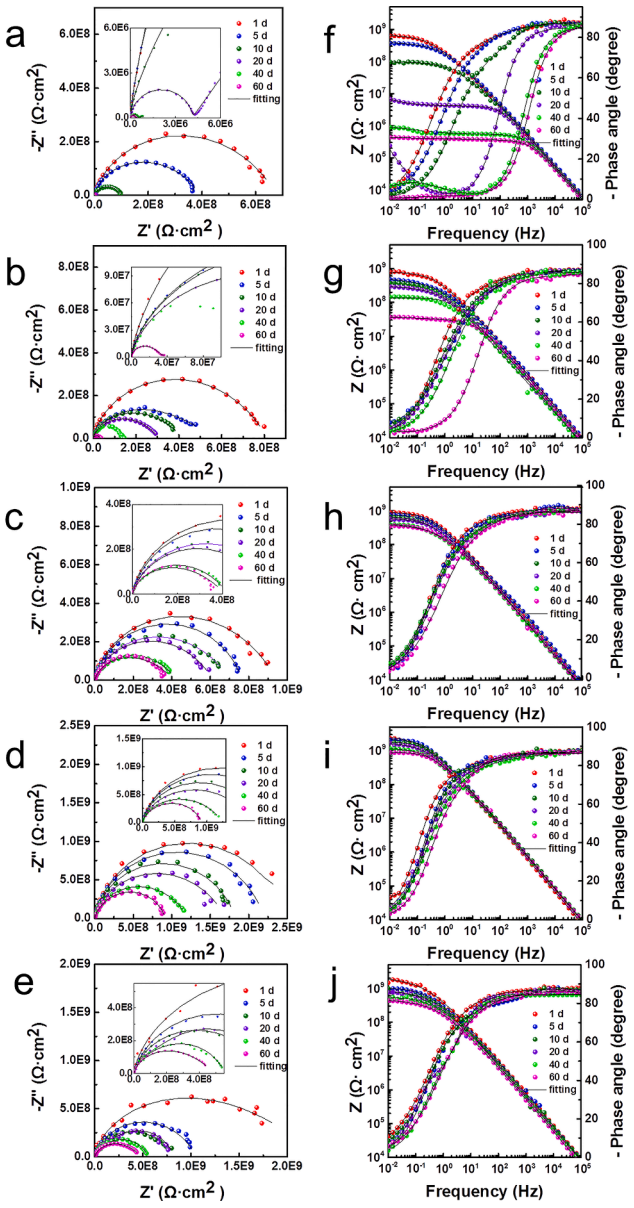


**Fig. 3.** The EIS results of (a) (f) pure EP, (b) (g) 0.5f-$Ti_3C_2T_X$/EP, (c) (h) 0.25SF-$Ti_3C_2T_X$/EP, (d) (i) 0. 5SF-$Ti_3C_2T_X$/EP and (e) (j) 0.75SF-$Ti_3C_2T_X$/EP coatings at different immersion time in the 3.5 wt% NaCl solution.

interface. The EIS results illustrated that the contraction of capacitive arc and the decrease of $|Z|_{0.01\ Hz}$. Moreover, the $|Z|_{0.01\ Hz}$ of the EP coating jumped down from $1.68 \times 10^8\ \Omega{\cdot}cm^2$ (96 h) to $2.35 \times 10^6\ \Omega{\cdot}cm^2$ (144 h), manifesting that the coating emerged the extensive blister under the acceleration of high hydrostatic pressure and the coating failed almost. At the end of the test, the coating lost the ability to protect the substrate. In addition, pure EP exhibited the resistive response and occupied a wider frequency range with soaking time increased, as shown in Fig. 5c. In the case of 0.5f-$Ti_3C_2T_X$/EP, Nyquist plots displayed diffusion arc after the 144 h immersion, compared with pure EP, the time delayed about 96 h, as shown in Fig. 5d. Besides, the value of $|Z|_{0.01\ Hz}$ remained $1.36 \times 10^6\ \Omega{\cdot}cm^2$ and two orders of magnitude higher than the pure EP during 240 h immersion, as shown in Fig. 5e. The 0.5f-$Ti_3C_2T_X$/EP was not complete failure. Unsurprisingly, 0.5SF-$Ti_3C_2T_X$/EP still maintained one capacitive arc during the 240 h immersion under 20 MPa hydrostatic pressure, as shown in Fig. 5g. Furthermore, value of $|Z|_{0.01\ Hz}$ up to $1.31 \times 10^8\ \Omega{\cdot}cm^2$ and four orders of magnitude higher than the pure EP, as shown in Fig. 5h. And 0.5SF-$Ti_3C_2T_X$/EP revealed a

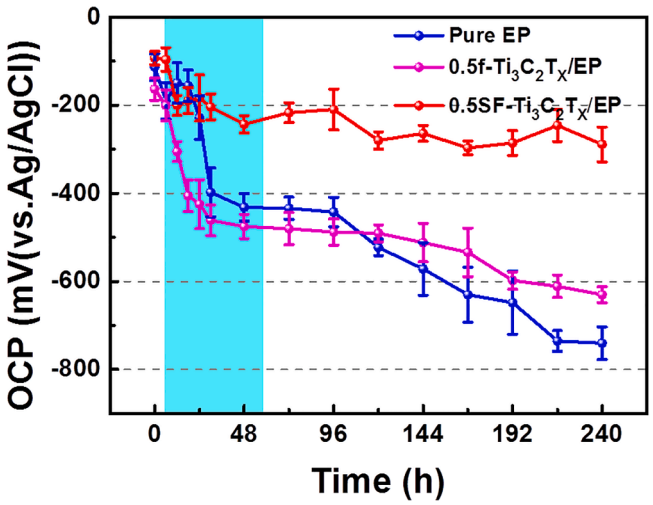


**Fig. 4.** The OCP of pure EP, f-$Ti_3C_2T_X$/EP and SF-$Ti_3C_2T_X$/EP.

steady capacitive response in wider frequency range, and the corresponding phase angle was closed to 90°, indicating that no or only slight corrosion reactions occurred on the substrate (Fig. 5i). Obviously, 0.5SF-$Ti_3C_2T_X$/EP could provide the excellent protection ability for steel, which was mainly due to that SF-$Ti_3C_2T_X$ could improve the compactness of resin and play an outstanding barrier property. These data were consistent with that of under atmospheric pressure, manifesting SF-$Ti_3C_2T_X$ great anticorrosion performance both of under atmospheric pressure and high hydrostatic pressures. The EIS data revealed that the failure process of coating was accelerated under hydrostatic pressure, but the introduction of SF-$Ti_3C_2T_X$ nanofiller could defer the failure effectively.

To further explore the protection behavior of the coating under hydrostatic pressure, the corresponding equivalent circuit models R(Q(R(QR))) and R(Q(R(Q(RW)))) were established by Zsimpwin software to fit the EIS data. In the equivalent circuit model includes $R_s$ (solution resistance), $R_c$ (coating resistance), $R_{ct}$ (charge transfer resistance), $Q_c$ (coating capacitance) and $Q_{dl}$ (double-layer capacitance) [43]. Besides, Warburg element (W) represented linear semi-infinite diffusion [44]. The results of $R_c$ and $C_c$ were shown in Fig. 6. The equivalent circuit could be selected equivalent circuit model B (Fig. 6a) while the barrier layer diffused or the corrosive medium reached the coating/metal interface (even corrosion reaction occurred). Under high hydrostatic pressure, due to inherent defects of waterborne epoxy resin, corrosion ions would penetrate into the coating in a short time or even reach the metal surface, resulting in electrochemical corrosion. Compared with the composite coating, the penetration time of pure EP coating was shorter, which was attributed to micro-defects in the pure EP coating. The 0.5f-$Ti_3C_2T_X$/EP exhibited a similar phenomenon, which was mainly due to the uneven distribution of f-$Ti_3C_2T_X$ in the epoxy matrix and limited the physical shielding effect. Therefore, the EIS data of pure EP after 48 h and 0.5f-$Ti_3C_2T_X$/EP after 144 h were fitted via model B.

The coating resistance $R_c$ was one of the crucial parameters to indicate the anti-corrosion performance of coatings [45]. Due to the invasion of corrosive medium or the increase of corrosion area, $R_c$ was inevitably decreased under high hydrostatic pressure. The $R_c$ of pure EP displayed two sharp decrease, as shown in Fig. 6b. The first stage was the decrease of $R_c$ from $9.3 \times 10^8\ \Omega{\cdot}cm^2$ to $9.5 \times 10^7\ \Omega{\cdot}cm^2$, from 0 h to 48 h. A proposed explanation for this phenomenon might be that the corrosive ions could open the channel and reach the coating/metal interface in a short time under water pressure. The second stage was the decrease of $R_c$ from $5.2 \times 10^7\ \Omega{\cdot}cm^2$ to $7.7 \times 10^3\ \Omega{\cdot}cm^2$, from 96 h to 240 h. With the accumulation of corrosion products and large scale blister of coating, the coating fail and lost the ability to protect the substrate. However, 0.5SF-$Ti_3C_2T_X$/EP retained the highest $R_c$ during

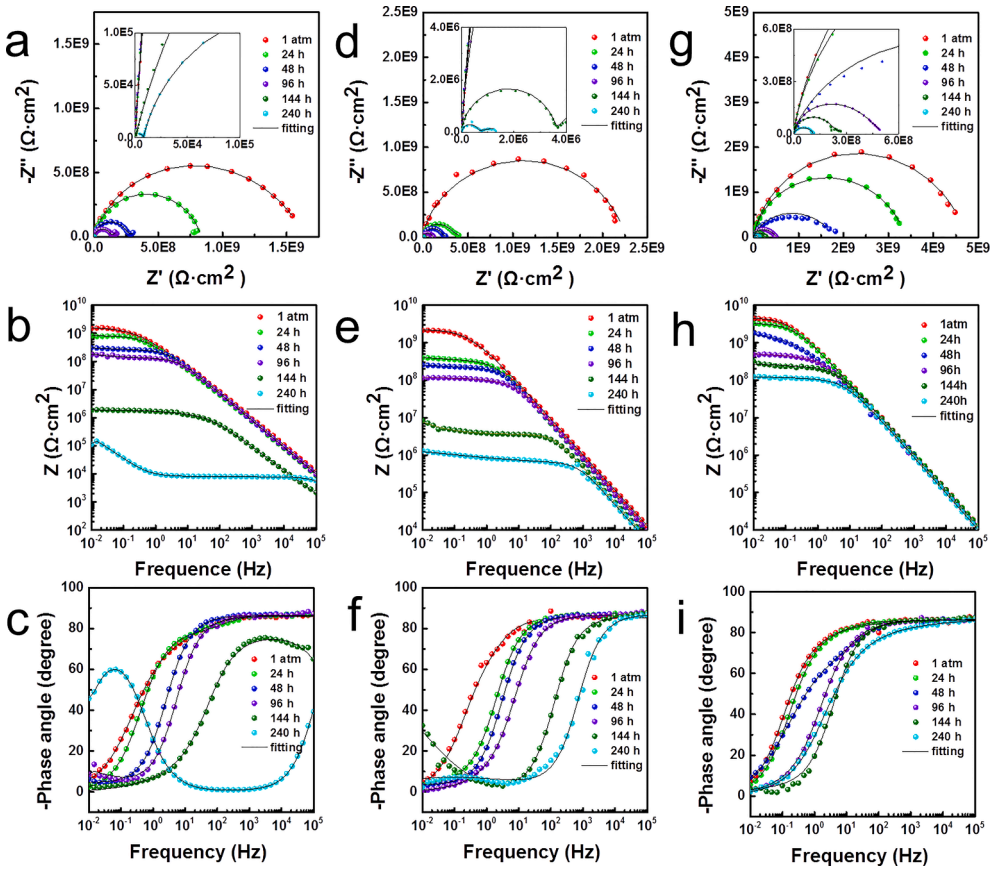


**Fig. 5.** The EIS results of (a) (b) (c) pure EP, (d) (e) (f) 0.5f-$Ti_3C_2T_X$/EP and (g) (h) (i) 0.5SF-$Ti_3C_2T_X$/EP coatings at different immersion time under 20 MPa hydrostatic pressure.

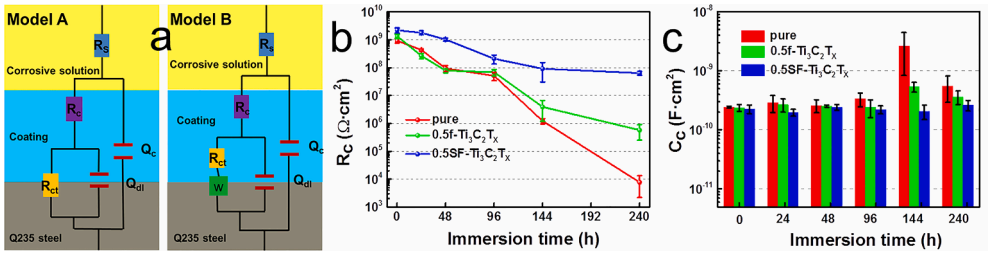


**Fig. 6.** (a) Equivalent electric circuit model; (b) $R_c$ and (c) $C_c$ for the as-prepared coatings under 20 MPa hydrostatic pressure.

the whole immersion period, indicating the coating displaying the excellent barrier performance under high pressure. In addition, the coating capacitance $C_c$ was the important information to evaluate the water-uptake behavior of coating [46]. As shown in Fig. 6c, the $C_c$ of coatings appeared an increased trend, inferring the coating continuously absorbed water under pressure. It could be observed that $C_c$ of pure EP rapidly increased from $2.42 \times 10^{-10}$ to $5.54 \times 10^{-10}$ F·cm$^{-2}$ with immersion. The sharp increase at 144 h may be due to the failure of the coating by high hydrostatic pressure. For the 0.5f-$Ti_3C_2T_X$/EP, the raise range was shrunken, which increased from $2.38 \times 10^{-10}$ to $3.61 \times 10^{-10}$ F·cm$^{-2}$. Moreover, the $C_c$ of 0.5SF-$Ti_3C_2T_X$/EP exposed a steady and slow growth, which increased from $2.25 \times 10^{-10}$ to $2.61 \times 10^{-10}$ F·cm$^{-2}$. This was attributed to the SF-$Ti_3C_2T_X$ nanosheets endued coating an outstanding barrier properties.

### 3.4. Characterizations of corrosion morphology

After 240 h of immersion under 20 MPa hydrostatic pressure, the corrosion production and surface morphologies of the Q235 steel surface were analyzed by the SEM, which could provide further insights illustrating the corrosion process. Generous and loose corrosion products and considerable pitting were appeared on the surface coated with pure EP was shown in Fig. 7a. The morphology confirmed that the coating was destroyed under pressure and the substrate occurred a serious electrochemical corrosion during the immersion process. Obviously, with the addition of the f-$Ti_3C_2T_X$ nanosheets, the corrosion degree of the substrate was decreased and the content of O and Cl element were declined, as shown in Fig. 7b. This indicated that f-$Ti_3C_2T_X$ nanosheets could suppress the penetration of corrosive molecules for a certain degree. Noteworthy, the surface coated with 0.5SF-$Ti_3C_2T_X$/EP was smooth and integrity without obvious corrosion regions and content O and Cl element were greatly reduced or even disappeared (Fig. 7c). The results suggested that the composite coating exhibited excellent corrosion resistance and the slightest corrosion degree. Based on these results, it could be concluded that the corrosion mediums diffusion were delayed by SF-$Ti_3C_2T_X$ nanosheets and endowed the coating with long-term

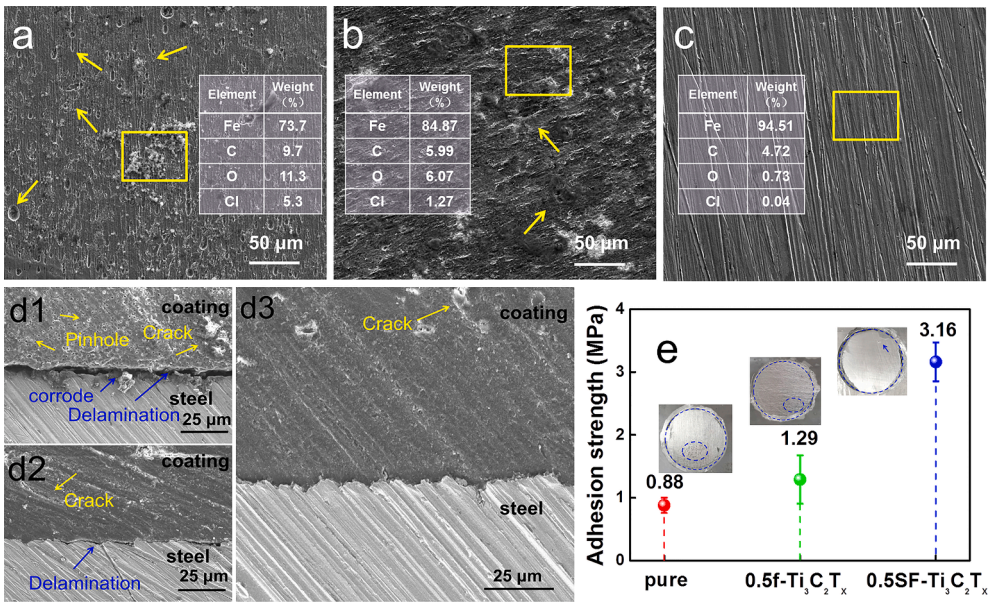


**Fig. 7.** Corrosion morphologies of (a) pure EP, (b) 0.5f-$Ti_3C_2T_X$/EP and (c) 0.5SF-$Ti_3C_2T_X$/EP; (d) SEM images of coating/steel interface; (e) the adhesion strength of pure EP, 0.5f-$Ti_3C_2T_X$/EP and 0.5SF-$Ti_3C_2T_X$/EP after 240 h immersion under 20 MPa hydrostatic pressure.

protection even under 20 MPa hydrostatic pressure.

### 3.5. Analysis the interface of coating/steel

The interface of coating/steel was critical to evaluate the coating's anti-corrosion performance [47]. The coating/steel interface of all coatings was observed via SEM after immersion for 240 h under 20 MPa hydrostatic pressure, as shown in the Fig. 7d. Noticeably, the pure EP (Fig. 7d1) appeared apparent pinholes and cracks after immersion, suggesting that the pure EP without the nanofiller was inferior and meaning the poor protection ability. Besides, the interface between pure EP/steel has presented delamination, inferring that the electrolyte reached the interface and serious corrosion occurred, leading to the failure of coating under water pressure. With the introduction of f-$Ti_3C_2T_X$, the compactness of the coating was improved and appeared slight interface delamination, as shown in Fig. 7d2. The coating was integrity and absence of delamination on the interface with added SF-$Ti_3C_2T_X$, meaning that the SF-$Ti_3C_2T_X$ nanosheets endowed the coating for ability to against aggression of corrosive medium under high hydrostatic pressure.

Furthermore, the adhesion strength of coatings was evaluated after being immersed for 240 h under 20 MPa pressure, as shown in the Fig. 7e. The order of adhesion strength was 0.5SF-$Ti_3C_2T_X$/EP (3.16 MPa) > 0.5f-$Ti_3C_2T_X$/EP (1.29 MPa) > pure EP (0.88 MPa). Besides, the steel surface coated with pure EP and 0.5f-$Ti_3C_2T_X$/EP appeared numerous corrosion marks. The result reflected that 0.5SF-$Ti_3C_2T_X$/EP still showed strong ability to protect metal substrate when confronting high hydrostatic pressure.

### 3.6. LEIS test

LEIS was an efficient method to evaluate the local corrosion of steel substrate, which was very sensitive to the local defects [48]. Before the test, a scratch (approximately 2 mm) was artificially made on the coating to evaluate the protective ability of the coating in the case of accelerated corrosion. At the defect area, the corrosive medium could instantaneously reach the metal surface and then trigger the local corrosion, so the impedance values around the scratch would be obviously lower than that of the undamaged area [49]. The LEIS results of the coated electrode with artificial defect during immersion in 3.5 wt% NaCl solution for 48 h were shown in the Fig. 8. In the spectrum, from red to green to blue and then to purple indicated that the local impedance value decreasing, which meant that the corrosion was deteriorated. Obviously, the impedance value of pure EP coating (Fig. 8a) was relatively low during the test. The impedance value of EP coating was decreased from 4 h to 48 h (the scratch area turned to be purple gradually), which illustrated that the corrosion ions initiated anodic reaction and facilitated the corrosion of metal. Besides, the dark blue and purple area was enlarged, which indicated that the barrier effect of the pure EP was poor and the corrosion medium was easy to diffuse. For the f-$Ti_3C_2T_X$/EP (Fig. 8b), the blue and purple area was significantly smaller than that of pure EP, suggesting that the f-$Ti_3C_2T_X$ nanosheets could delay the invasion of corrosive mediums and slow down the corrosion reaction to a certain extent. With the addition of SF-$Ti_3C_2T_X$ (Fig. 8c, 8d and 8e), the LEIS image did not appear blue and only showed a little green even after 48 h of immersion. Particularly, 0.5SF-$Ti_3C_2T_X$/EP exhibited the highest impedance value and the smallest corrosion area. These results revealed that the SF-$Ti_3C_2T_X$ endowed epoxy resin excellent protection ability. Obviously, when the coating had artificial defect, the impedance of pure EP and f-$Ti_3C_2T_X$/EP coating decreased fast, and the area affected by the defect was large. However, the SF-$Ti_3C_2T_X$/EP coating was slightly affected by the artificial defect, indicating the excellent protection ability of the coating.

### 3.7. Corrosion protection mechanism

The compactness of the coating was the key to provide a favorable physical shielding property. The form of pinhole was inevitable in the curing process of the general polymer coating, which would lead to a decrease in the protection efficiency of the coating. However, the introduction of 2D nanofiller could prolong the diffusion path of the corrosive medium to a certain extent and slow down the corrosion of the metal matrix. Based the data above, the corrosion protection mechanism of the pure EP, 0.5f-$Ti_3C_2T_X$/EP and 0.5SF-$Ti_3C_2T_X$/EP were be analyzed, the schematic diagram was exhibited in Fig. 9. At atmospheric pressure, due to the existence of $Ti_3C_2T_X$ nanosheets, a physical barrier network would be form in the composite coating, which could prolong the diffusion channel of corrosive medium and provide long-term protection for metal. However, for the pure EP, due to its own defects, would gradually lose its protection ability due to the erosion and

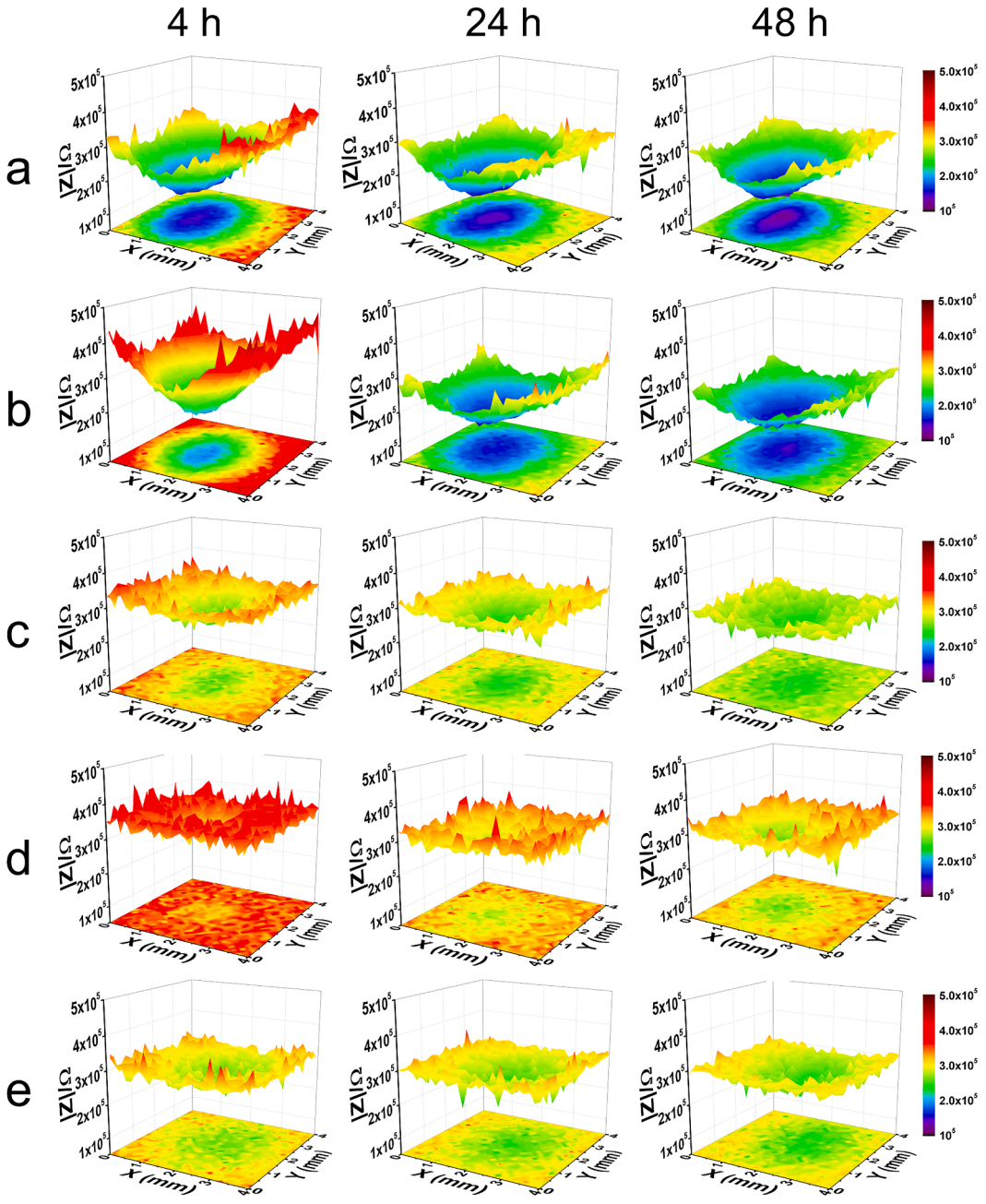


**Fig. 8.** LEIS test results of (a) pure EP, (b) 0.5f-$Ti_3C_2T_X$/EP, (c) 0.25SF-$Ti_3C_2T_X$/EP, (d) 0.5SF-$Ti_3C_2T_X$/EP and (e) 0.75SF-$Ti_3C_2T_X$/EP coatings in the 3.5 wt% NaCl solution after 48 h immersion.

diffusion of corrosive ions in the immersion process. For the pure EP, continuous cracks and defects would be formed under hydrostatic pressure, which would open the corrosion channel and cause the substrate to be eroded by corrosion ions. With prolonging the immersion time, the coating absorbed water and blistered, which led to rapid failure under high hydrostatic pressure, eventually. Due to the f-$Ti_3C_2T_X$, the cracks formation was discontinuous under high hydrostatic pressure and the physical barrier effect of f-$Ti_3C_2T_X$ nanosheets delayed the corrosive ions penetrated into coating. But the physical shielding effect was limited by the agglomeration of the nanosheets, so the coating would absorb water gradually fail under high hydrostatic pressure and reduced the protection performance. The 0.5SF-$Ti_3C_2T_X$/EP displayed favorable dispersity and interfacial compatibility of SF-$Ti_3C_2T_X$, which the coating formed a dense protective layer and an effective barrier net. In addition, SF-$Ti_3C_2T_X$ nanosheets had the ability to prevent further cracks propagation. Thus, the diffusion rate of the corrosive medium was greatly slowed down and the coating remained intact under high hydrostatic pressure.

## 4. Conclusions

Herein, we designed and synthesized a novel SF-$Ti_3C_2T_X$ hybrid nanofiller, which was incorporated into waterborne coatings to improve the comprehensive anticorrosion performance of the coating. The as-prepared SF-$Ti_3C_2T_X$ hybrid exhibited excellent dispersion in epoxy resin, which effectively filled the inherent holes and defects in matrix and significantly prolonged the diffusion path of the corrosive medium in the coating. Meanwhile, the protein fiber on the surface of SF-$Ti_3C_2T_X$ nanosheets was beneficial for interface bonding with the resin, which played a role of “pinning” and improved the mechanical properties of

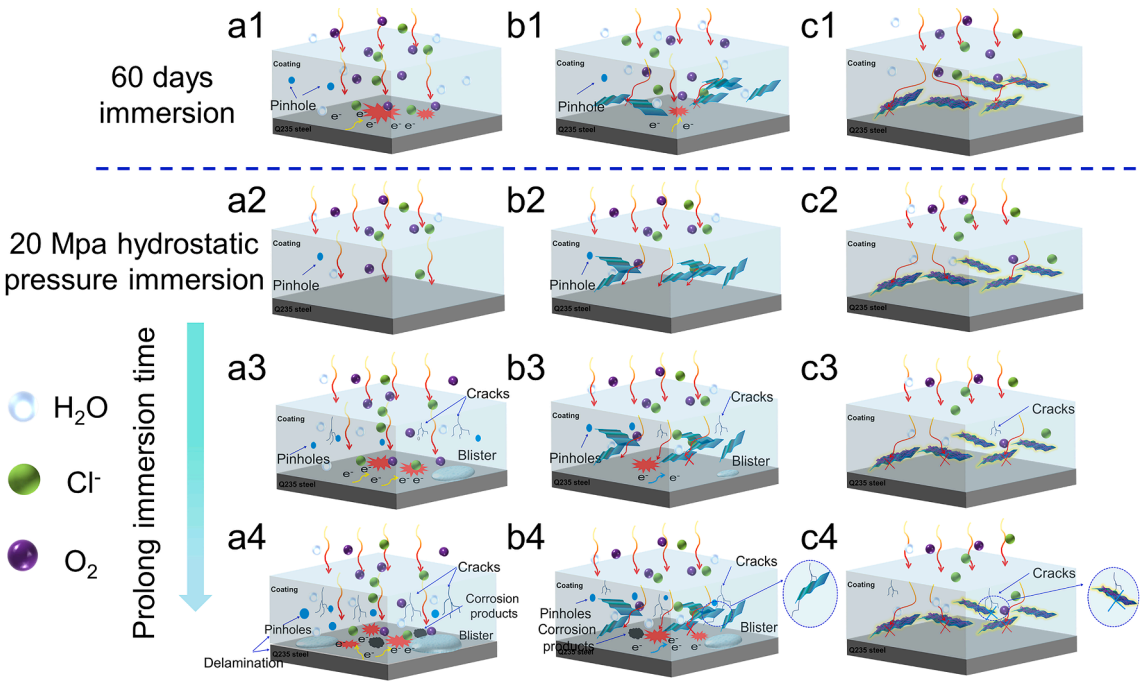


**Fig. 9.** The schematic diagram of corrosion mechanism for (a) pure EP, (b) 0.5f-$Ti_3C_2T_X$/EP and (c) 0.5SF-$Ti_3C_2T_X$/EP.

the EP resin. In addition, the appropriate addition of SF-$Ti_3C_2T_X$ (0.5 wt %) was conducive to achieve more excellent corrosion resistance. Indeed, 0.5SF-$Ti_3C_2T_X$/EP displayed the excellent adhesion strength (5.4 MPa, but that of pure EP was 2.21 MPa). Moreover, the 0.5SF-$Ti_3C_2T_X$/EP still displayed the excellent anti-corrosion performance after immersion for 60 days under atmospheric pressure. Notably, the $|Z|_{0.01\ Hz}$ of 0.5SF-$Ti_3C_2T_X$/EP still maintained $\sim 10^8\ \Omega\cdot cm^2$ (four orders of magnitude higher than the pure EP) after immersion for 240 h under severe hydrostatic pressure. Hence, the as-prepared SF-$Ti_3C_2T_X$ hybrid was not only entrust to the coating long-term anti-corrosion ability, but also shows an outstanding ability of protection and defer failure in the face of harsh deep-sea environment.

## Declaration of Competing Interest

The authors declare that they have no known competing financial interests or personal relationships that could have appeared to influence the work reported in this paper.

## Acknowledgements

This research was supported by Zhejiang Provincial Natural Science Foundation of China (LR21E050001), Key Research Program of Frontier Sciences of the Chinese Academy of Sciences (QYZDY-SSW-JSC009), and Youth Innovation Promotion Association, CAS (No.2017338).

## Appendix A. Supplementary data

Supplementary data to this article can be found online at https://doi.org/10.1016/j.cej.2021.130195.

## References

[1] W. Tian, L. Liu, F. Meng, Y. Liu, Y. Li, F. Wang, The failure behaviour of an epoxy glass flake coating/steel system under marine alternating hydrostatic pressure, Corros. Sci. 86 (2014) 81–92.
[2] D.A. Shifler, Understanding material interactions in marine environments to promote extended structural life, Corros. Sci. 47 (2005) 2335–2352.
[3] Y. Yang, T. Zhang, Y. Shao, G. Meng, F. Wang, Effect of hydrostatic pressure on the corrosion behaviour of Ni–Cr–Mo–V high strength steel, Corros. Sci. 52 (2010) 2697–2706.
[4] F. Meng, L. Liu, W. Tian, H. Wu, Y. Li, T. Zhang, F. Wang, The influence of the chemically bonded interface between fillers and binder on the failure behaviour of an epoxy coating under marine alternating hydrostatic pressure, Corros. Sci. 101 (2015) 139–154.
[5] B. Liu, Z.G. Fang, H.B. Wang, T. Wang, Effect of cross linking degree and adhesion force on the anti-corrosion performance of epoxy coatings under simulated deep sea environment, Prog. Org. Coat. 76 (2013) 1814–1818.
[6] L. Liu, Y. Cui, Y. Li, T. Zhang, F. Wang, Failure behavior of nano-$SiO_2$ fillers epoxy coating under hydrostatic pressure, Eletrochim. Acta 62 (2012) 42–50.
[7] Y. Liu, J. Wang, L. Liu, Y. Li, F. Wang, Study of the failure mechanism of an epoxy coating system under high hydrostatic pressure, Corros. Sci. 74 (2013) 59–70.
[8] M. Nematollahi, M. Heidarian, M. Peikari, S.M. Kassiriha, N. Arianpouya, M. Esmaeilpour, Comparison between the effect of nanoglass flake and montmorillonite organoclay on corrosion performance of epoxy coating, Corros. Sci. 52 (2010) 1809–1817.
[9] F. Meng, T. Zhang, L. Liu, Y. Cui, F. Wang, Failure behaviour of an epoxy coating with polyaniline modified graphene oxide under marine alternating hydrostatic pressure, Surf. Coat. Technol. 361 (2019) 188–195.
[10] N.T. Kirkland, T. Schiller, N. Medhekar, N. Birbilis, Exploring graphene as a corrosion protection barrier, Corros. Sci. 56 (2012) 1–4.
[11] Y. Wu, W. Zhao, Y. Qiang, Z. Chen, L. Wang, X. Gao, Z. Fang, π-π interaction between fluorinated reduced graphene oxide and acridizinium ionic liquid: Synthesis and anti-corrosion application, Carbon 159 (2020) 292–302.
[12] Y. Ye, D. Zhang, J. Li, T. Liu, J. Pu, H. Zhao, L. Wang, One-step synthesis of superhydrophobic polyhedral oligomeric silsesquioxane-graphene oxide and its application in anti-corrosion and anti-wear fields, Corros. Sci. 147 (2019) 9–21.
[13] J. Ding, H. Zhao, X. Zhao, B. Xu, H. Yu, How semiconductor transition metal dichalcogenides replaced graphene for enhancing anticorrosion, J. Mater. Chem. A. 7 (2019) 13511–13521.
[14] L. Shen, Y. Zhao, Y. Wang, R. Song, Q. Yao, S. Chen, Y. Chai, A long-term corrosion barrier with an insulating boron nitride monolayer, J. Mater. Chem. A. 4 (2016) 5044–5050.
[15] M. Sun, S. Xu, L. Zhao, B. Zhang, Fabrication of oriented layered double hydroxide films by spin coating and their use in corrosion protection, Chem. Eng. J. 141 (2008) 362–367.
[16] W. Wang, H. Wang, J. Zhao, X. Wang, C. Xiong, L. Song, R. Ding, P. Han, W. Li, Self-healing performance and corrosion resistance of graphene oxide–mesoporous silicon layer–nanosphere structure coating under marine alternating hydrostatic pressure, Chem. Eng. J. 361 (2019) 792–804.
[17] Y. Ye, D. Zhang, T. Liu, Z. Wei, J.P.H. Chen, H. Zhao, X. Li, Improvement of anticorrosion ability of epoxy matrix in simulate marine environment by filled with superhydrophobic POSS-GO nanosheets, J. Hazard. Mater. 141 (2008) 362–367.
[18] B. Ramezanzadeh, A. Ahmadi, M. Mandavian, Enhancement of the corrosion protection performance and cathodic delamination resistance of epoxy coating through treatment of steel substrate by a novel nanometric sol-gel based silane composite film filled with functionalized graphene oxide nanosheets, Corros. Sci. 109 (2016) 182–205.

[19] M. Cui, S. Ren, J. Chen, S. Liu, G. Zhang, H. Zhao, L. Wang, Q. Xue, Anticorrosive performance of waterborne epoxy coatings containing water-dispersible hexagonal boron nitride (h-BN) nanosheets, Appl. Surf. Sci. 397 (2016) 77–86.
[20] D. Er, J. Li, M. Naguib, Y. Gogotsi, V.B. Shenoy, MXenes as high capacity electrode materials for metal (Li, Na, K, Ca)-ion batteries, ACS Appl. Mater. Interfaces. 6 (2014) 11173–11179.
[21] Y.H. Li, F. Zhang, Y. Chen, J.Y. Li, Y. Xu, Photoredox-catalyzed biomass intermediate conversion integrated with $H_2$ production over $Ti_3C_2T_X$/CdS composites, ACS Nano 22 (2020) 163–169.
[22] Tianran Ting-HsiangChang, Haitao Zhang, Kerui Yang, Yuan Li, Controlled crumpling of two-dimensional titanium carbide (MXene) for highly stretchable, bendable, efficient supercapacitors, ACS Nano 12 (2018) 8048–8059.
[23] X. Xie, N. Zhang, Z.R. Tang, M. Anpo, Y.J. Xu, $Ti_3C_2T_X$ MXene as a Janus cocatalyst for concurrent promoted photoactivity and inhibited photocorrosion, Appl. Catal. B Environ. 237 (2018) 43–49.
[24] X. Xie, C. Chen, N. Zhang, Z.R. Tang, Y. Xu, Microstructure and surface control of MXene films for water purification, Nat. Sustain. 2 (2019) 856–862.
[25] M. Naguib, M. Kurtoglu, V. Presser, J. Lu, J. Niu, M. Heon, L. Hultman, Y. Gogotsi, M.W. Barsoum, Two-dimensional nanocrystals produced by exfoliation of $Ti_3AlC_2$, Adv. Mater. 331 (2011) 4248–4253.
[26] M. Naguib, V.N. Mochalin, M.W. Barsoum, Y. Gogotsi, 25th anniversary article: MXenes: A new family of two-dimensional materials, Adv. Mater. 26 (2014) 992–1005.
[27] B. Anasori, Y. Xie, M. Beidaghi, J. Lu, B.C. Hosler, L. Hultman, P.R.C. Kent, Y. Gogotsi, M.W. Barsoum, Two-Dimensional, Ordered, Double Transition Metals Carbides (MXenes), Acs Nano 9 (2015) 9507–9516.
[28] M. Malaki, R.S. Varma, Mechanotribological aspects of mxene-reinforced nanocomposites, Adv. Mater. (2020), 2003154.
[29] H. Yan, W. Li, H. Li, X. Fan, M. Zhu, $Ti_3C_2$ MXene nanosheets toward high-performance corrosion inhibitor for epoxy coating, Prog. Org. Coat. 135 (2019) 156–167.
[30] Y. Ye, D. Zhang, T. Liu, Z. Liu, J. Pu, W. Liu, H. Zhao, X. Li, L. Wang, Superior corrosion resistance and self-healable epoxy coating pigmented with silanzied trianiline-intercalated graphene, Carbon 142 (2019) 164–176.
[31] H. Yan, M. Cai, W. Li, X. Fan, M. Zhu, Amino-functionalized $Ti_3C_2T_X$ with anti-corrosive/wear function for waterborne epoxy coating, J. Mater. Sci. Tech. 54 (2020) 144–159.
[32] H. Yan, L. Zhang, H. Li, X. Fan, M. Zhu, Towards high-performance additive of $Ti_3C_2$/graphene hybrid with a novel wrapping structure in epoxy coating, Carbon 157 (2020) 217–233.
[33] P. Bhattacharjee, B. Kundu, D. Naskar, H.W. Kim, T.K. Maiti, D. Bhattacharya, S. C. Kundu, Silk scaffolds in bone tissue engineering: An overview, Acta Biomater. 63 (2017) 1–17.
[34] B. Zhu, H. Wang, W.R. Leow, Y. Cai, X.J. Loh, M.Y. Han, X. Chen, Silk fibroin for flexible electronic devices, Adv. Mater. 28 (2016) 4250–4265.
[35] J. Chen, W. Zhao, Simple method for preparing nanometer thick $Ti_3C_2T_X$ sheets towards highly efficient lubrication and wear resistance, Tribol. Inter. 153 (2021), 106598.
[36] M. Boota, B. Anasori, C. Voigt, M.Q. Zhao, M.W. Barsoum, Y. Gogotsi, Pseudocapacitive electrodes produced by oxidant-free polymerization of pyrrole between the layers of 2D titanium carbide (MXene), Adv. Mater. 28 (2016) 1517–1522.
[37] Q. Xue, H. Zhang, M. Zhu, Z. Pei, H. Li, Z. Wang, Y. Huang, Y. Huang, Q. Deng, J. Zhou, Photoluminescent $Ti_3C_2$ MXene Quantum Dots for Multicolor Cellular Imaging, Adv. Mater. 29 (2017) 1604847.1–1604847.6.
[38] B. Ahmed, D.H. Anjum, M.N. Hedhili, Y. Gogotsi, H. Alshareef, $H_2O_2$ assisted room temperature oxidation of $Ti_2C$ MXene for Li-ion battery anodes, Nanoscal 8 (2016) 7850–7857.
[39] W. Sun, L. Wang, T. Wu, M. Wang, Z. Yang, Y. Pan, G. Liu, Inhibiting the corrosion-promotion activity of graphene, Chem. Mater. 27 (2015) 2367–2373.
[40] Z. Mirzakhanzadeh, A. Kosari, M.H. Moayed, R. Naderi, P. Taheri, J.M.C. Mol, Enhanced corrosion protection of mild steel by the synergetic effect of zinc aluminum polyphosphate and 2-mercaptobenzimidazole inhibitors incorporated in epoxy-polyamide coatings, Corros. Sci. 138 (2018) 372–379.
[41] Y. Ye, D. Yang, D. Zhang, H. Chen, L. Wang, POSS-tetraaniline modified graphene for active corrosion protection of epoxy-based organic coating, Chem. Eng. J. 383 (2019), 123160.
[42] Y. Qiang, S. Zhang, H. Zhao, B. Tan, L. Wang, Enhanced anticorrosion performance of copper by novel N-doped carbon dots, Corros. Sci. 161 (2019), 108193.
[43] L. Shen, Y. Li, W.J. Zhao, K. Wang, X.J. Ci, Y.M. Wu, G. Liu, C. Liu, Z.W. Fang, Tuning F-doped degree of rGO: Restraining corrosion-promotion activity of EP/rGO nanocomposite coating, J. Mater. Sci. Tech. 44 (2020) 121–132.
[44] Y. Wu, F. Jiang, Y. Qiang, W. Zhao, Synthesizing a novel fluorinated reduced graphene oxide-CeO 2 hybrid nanofiller to achieve highly corrosion protection for waterborne epoxy coatings, Carbon 176 (2021) 39–51.
[45] J. Ding, H. Zhao, B. Xu, X. Zhao, S. Su, H. Yu, Superanticorrosive Graphene Nanosheets through π Deposition of Boron Nitride Nanodots, ACS Sustain. Chem, Eng, 2019.
[46] F. Deflorian, L. Fedrizzi, S. Rossi, P.L. Bonora, Organic coating capacitance measurement by EIS: ideal and actual trends, Eletrochim. Acta 44 (1999) 4243–4249.
[47] W. Tian, F. Meng, L. Liu, Y. Li, F. Wang, The failure behaviour of a commercial highly pigmented epoxy coating under marine alternating hydrostatic pressure, Prog. Org. Coat. 82 (2015) 101–112.
[48] Y. Su, S. Qiu, D.Yang, S. Liu, H. Zhao, L. Wang, Q. Xue, Active anti-corrosion of epoxy coating by nitrite ions intercalated mgal LDH. J. Hazard. Mater. 391(21), 122215.
[49] T. Ge, W. Zhao, X. Wu, X. Lan, Y. Zhang, Y. Qiang, Y. He, Incorporation of electroconductive carbon fibers to achieve enhanced anti-corrosion performance of zinc rich coatings, J. Colloid Interf. Sci. 567 (2020) 113–125.